JOURNAL OF PROPULSION AND POWER
Vol. 29, No. 3, May–June 2013

Thrust Measurements of a Radio Frequency Plasma Source

Logan T. Williams* and Mitchell L. R. Walker†
Georgia Institute of Technology, Atlanta, Georgia 30332

DOI: 10.2514/1.B34574

There is interest in the use of a helicon plasma source in propulsive applications as both an ion source and a thruster. Development of a helicon thruster requires a performance baseline as a basis for future optimization and modification. For the first time, the thrust of a helicon plasma source is measured using a null-type inverted pendulum thrust stand at an operating pressure of 2×10^{-5} torr through the operating range of 215–840 W RF power, 11.9 and 13.56 MHz RF frequency, 150–450 G magnetic field strength, and 1.5–4.5 mg/s propellant flow rate for argon. Maximum thrust is found to be 6.3 mN at a specific impulse of 140 s and a maximum specific impulse of 380 s at 5.6 mN. Thrust efficiency is less than 1.4% and demonstrates very-low-power coupling to ion acceleration.

Nomenclature

d	=	diameter of the discharge chamber, m
e	=	charge of an electron, C
g	=	acceleration due to gravity, m · s^{-2}
I_b	=	beam current, C · s^{-1}
I_c	=	collected ion current, C · s^{-1}
$I_{c,\max}$	=	maximum collected centerline ion current, C · s^{-1}
$I_{c,w}$	=	weighted collected centerline ion current, C · s^{-1}
$I_{\rm sp}$	=	specific impulse, s
m	=	propellant atomic mass, kg
$\dot{m}$	=	mass flow rate, kg · s^{-1}
m_i	=	ion mass, kg
p_b	=	base pressure, torr
p_g	=	ion gauge pressure, torr
$P_{\rm in}$	=	total input power to the device, W
p_o	=	operating pressure, torr
$P_{\rm RF}$	=	RF power input into the device, W
Q	=	volumetric flow rate of propellant, sccm
T	=	thrust, mN
V_b	=	beam voltage, V
V_j	=	jth voltage of the ion energy distribution function, V
V_p	=	plasma potential, V
v_i	=	ion exit velocity, km · s^{-1}
$\bar{v}$	=	average ion exit velocity, km · s^{-1}
x_j	=	probability of the jth voltage in the IEDF
η_t	=	thrust efficiency
χ	=	gas correction factor

I. Introduction

HELICONS have been studied as high-efficiency, high-density plasma sources since the 1960s [1–3]. A helicon plasma source is an RF plasma generator that operates by launching a helicon wave along an axial magnetic field. The wave couples to the plasma and deposits the RF power into the electrons. A helicon wave is a bounded right-hand circularly polarized electromagnetic wave with a frequency low enough that electron gyration can be neglected [1]. Helicon sources have been observed to create plasmas an order of magnitude denser than a dc gas discharge at the same input power [4]. The high ionization efficiency of the helicon source was previously attributed to Landau damping [1], but later work has considered Trivelpiece–Gould wave coupling as the primary mechanism [5,6].

Although there are several uses for helicon plasmas in terrestrial applications, such as plasma processing [7], there have also been studies considering helicon sources in space propulsion. Some research considers using the helicon source as an ion generator [8–11]; other work examines the possibility of the helicon source itself as a thruster [12–15]. There are limited experimental data on the measured performance of the helicon source as a thruster. Much of the research thus far has focused on plume measurements. Several published works [16,17] use a retarding potential analyzer (RPA) to characterize the ion energy distribution, which was found to have two primary peaks: one at the plasma potential and one at a higher potential. This higher-energy peak corresponds to ions accelerated across a potential drop that occurs along the axis of the device that is formed by a current-free expansion double layer [17,18]. Additional work examining the potential along the axis of symmetry of a helicon found that a higher magnetic field increased the magnitude of the potential drop experienced by the ions [19,20]. Later work used the RPA to measure the ion beam current density across a plane perpendicular to the axis of symmetry of the helicon [21]. Efforts to determine the thrust of the helicon include testing with a momentum flux target [22,23] and direct thrust measurements, which observed thrust in the range of 0–3 [24] and 1–2.8 [25] mN at powers up to 700 and 650 W, respectively. This work measures the thrust of a helicon plasma source with a null-type inverted pendulum thrust stand over a range of RF powers between 215 and 800 W, axial magnetic field strengths between 150 and 450 G, frequencies of 11.9 and 13.56 MHz, and mass flow rates between 1.5 and 4.5 mg/s of argon. The device used in this study is designed after a helicon source design found in the literature that was previously found to achieve helicon mode [26]. It is important to note the distinction between the device architecture and the plasma coupling mode; therefore, the device tested is referred to as a helicon plasma source due to its design, even if it may not always be operated in the helicon mode.

II. Experimental Apparatus

A. Vacuum Facilities

All experiments are conducted in Georgia Institute of Technology, High Power Electric Propulsion Lab, Vacuum Test Facility 1 (VTF-1). VTF-1 is a stainless steel vacuum chamber 4 m in diameter with a length of 7 m. Two 3800 CFM blowers and two 495 CFM rotary-vane pumps evacuate the chamber to a moderate vacuum (about 30 mtorr). High vacuum is normally reached by using six 48 in. diffusion pumps with a combined pumping speed of 485,000 1/s on argon. Because of the presence of optical baffles the effective pumping speed is 125,000 1/s. The chamber pressure is measured with a BA-571 ion

Presented as Paper 2011-5893 at the 47th AIAA/ASME/SAE/ASEE Joint Propulsion Conference and Exhibit, San Diego, CA, 31 July 2011–3 August 2011; received 30 January 2012; revision received 12 December 2012; accepted for publication 15 January 2013; published online 3 April 2013.

*Graduate Research Assistant, Aerospace Engineering, High-Power Electric Propulsion Laboratory; lwilliams@gatech.edu. Student Member AIAA.

†Associate Professor, Aerospace Engineering, High-Power Electric Propulsion Laboratory; mitchell.walker@ae.gatech.edu. Associate Fellow AIAA.

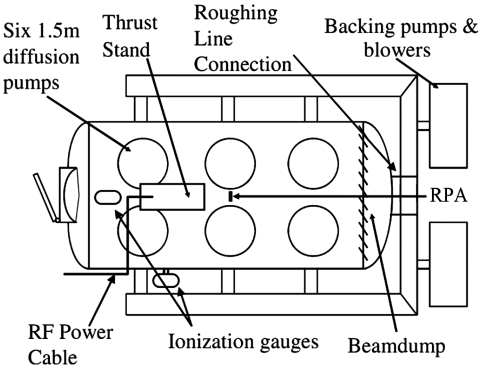

Fig. 1 VTF schematic.

gauge connected to a Varian Sentorr controller with an uncertainty of 20% [27]. An MKS type 247 four-channel readout in conjunction with an MKS 1179 mass flow controller regulates the gas flow into the helicon with an error of ±1% [28]. The base pressure of VTF-1 for these experiments is 1.5×10^{-5} torr. Figure 1 shows a schematic of the VTF.

Operating pressure p_o is derived by a correction of the pressure measured by the ion gauge, given by

$$p_o = \frac{p_g - p_b}{\chi} + p_b \tag{1}$$

where p_g is the pressure given by the ion gauge, p_b is the base pressure, and χ is the gas correction factor, which is 1.29 for argon.

B. Helicon Plasma Source

Figure 2 shows the geometry of the helicon plasma source and a schematic of the RF system. The helicon consists of a Pyrex discharge chamber 27.3 cm long and 14.0 cm in diameter. The axial magnetic field is provided by two 725 turn solenoids 7.6 cm wide with a 19.7 cm inner diameter. The solenoids are placed 10.2 cm apart. Figure 3 shows the on-axis magnetic field strength for the four solenoid currents used. The magnetic field strengths are referred to by the strength at the center of the antenna; thus, whereas the device is tested at solenoid currents of 3.76, 6.26, 8.75, and 11.25 A, it is referred to as 150, 250, 350, and 450 G, respectively. The RF signal is provided by a Yaesu FT-540 HF transceiver and amplified by an ACOM 2000A linear amplifier. A LP-100 RF wattmeter monitors the RF power transmitted and measures the standing wave ratio (SWR) with an uncertainty of ±1 W for power and ±0.05 for the SWR. The signal is matched by a π-type matching network. RF power is transmitted through an unbalanced coaxial cable of fixed length set by RF frequency to minimize RF leakage and power loss through the cable [29]. The signal is then transmitted into the plasma using a

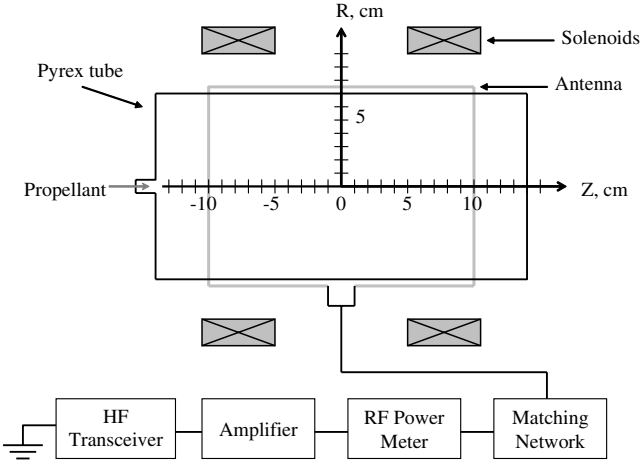

Fig. 2 Helicon configuration and RF schematic.

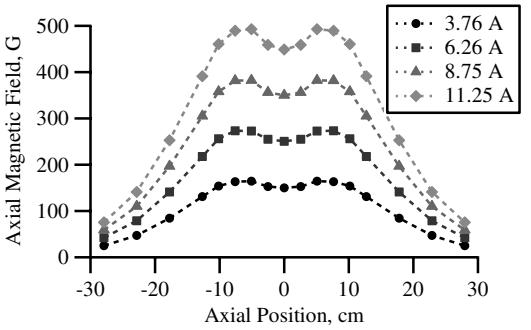

Fig. 3 Centerline axial magnetic field strength at four solenoid currents.

double saddle antenna centered between the solenoids. The attenuation of the transmission line is measured beforehand with a MFJ-269 SWR meter and used to correct the nominal power given by the wattmeter. The matched-line loss for 11.9 and 13.56 MHz is 0.8 and 1.5 dB, respectively, which includes attenuation caused by the feedthrough. During testing, the SWR ranged from 1.01 to 1.10, which results at most in an additional 0.004 and 0.010 dB of attenuation for 11.9 and 13.56 MHz, respectively. Examinations of similarly sized devices run at similar operating conditions suggest that much of the data was collected from an inductively coupled discharge mode [26,30]. Some operating points at the upper bound of the power range might correspond to helicon mode, though no observations of a blue core or measurements of the helicon wave are available to confirm.

The antenna used is a double saddle antenna designed similarly to the type used by Chi et al. [26]. The antenna is 20.3 cm long and 15.9 cm in diameter. The antenna is composed of copper strips 1.25 cm wide and 0.318 cm thick welded together. A gap of 0.635 cm separates the two terminals that are connected to the coax cable. The antenna is wrapped in fiberglass tape to prevent direct electrical contact between the antenna and any stray plasma or the solenoids. A CAD model of the antenna is shown in Fig. 4.

Because of the nature of the helicon, there are two issues that must be addressed during setup to ensure accurate thrust measurement. The first is thermal drift of the thrust stand due to thermal expansion of the RF cable. As the cable is heated during operation, the cable expands, pushing on the antenna and producing a growing offset to the measurements. To prevent this, the antenna is bolted to a three-axis bracing mount, which fixes the antenna in place such that it does not contact either the discharge chamber or the solenoids. In this configuration, the solenoids, discharge chamber, and propellant line are fixed to the thrust stand, whereas the antenna is isolated from the rest of the device and the thrust stand. The majority of the device can then move freely along the axis of motion of the thrust stand and through the antenna, which remains fixed. The propellant line is integrated into the thrust stand and does not affect the measurements. Additionally, the RF cable makes a roughly 270 deg spiral to the antenna in the plane perpendicular to the axis of motion of the thrust stand, allowing the cable to thermally expand along the arc, which prevents expansion into the antenna, which could reduce the

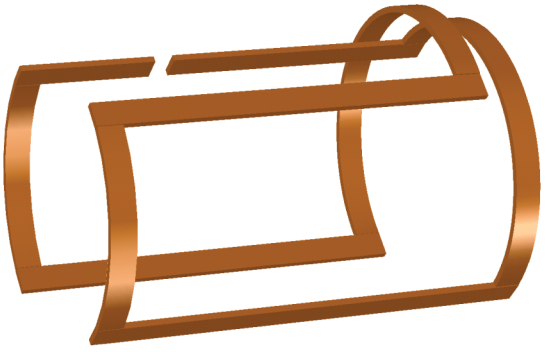

Fig. 4 CAD model of the double saddle antenna.

separation distance between the antenna and the discharge chamber. Thus, during operation, any thermal stress on the antenna is never transferred to the solenoids or the discharge chamber, and by extension the thrust stand, which eliminates thermal drift caused by the cable.

The second issue with measuring the thrust of a helicon on a thrust stand is eliminating any RF pickup in the thrust stand signal lines. An interfering RF signal appeared as a dc offset to the measured thrust stand null coil current required to maintain the thrust stand position whenever the helicon was turned on. This occurred even when the helicon was removed from the thrust stand and placed on the floor of the chamber 1 m away. This was ultimately a ground loop and shielding issue with the thrust stand electronics; the solution has two parts. Inside the chamber, all signal lines are isolated from chamber ground, whereas the cable shielding is grounded to prevent RF pickup. Outside the chamber, the signal lines are still isolated from chamber ground, but the cable shielding is tied to the thrust stand electronics common ground. Each electronic component of the thrust stand is placed in a grounded enclosure tied to the common ground, which is tied to the ground of a single wall outlet. This removed all RF offset during helicon operation, confirmed by operating the helicon on the thrust stand aligned orthogonal to the axis of motion of the thrust stand and observing no offset.

C. Diagnostics

1. *Thrust Stand*

The thrust of the helicon is measured with a null-type inverted pendulum thrust stand [31]. The thrust stand consists of two parallel plates connected by a series of four flexures, which support the upper plate and allow deflection as a force is applied. A linear variable differential transformer (LVDT) measures the position of the upper plate, whereas two electromagnetic actuators control the motion. One actuator, the damper coil, compensates for vibrations, and the second, the null coil, holds the upper plate stationary. The thrust stand operates by using two proportional-integral-derivative control circuits, which use the LVDT signal as input and the current through one of the actuators as the output. The resulting current through the null coil is directly correlated to the force required to maintain the position of the thrust stand and is calibrated by comparing the null coil current to the application of a series of known weights. The driving current in the null coil of the thrust stand is digitally recorded using a LabView virtual instrument program interfacing with a Keithley 2410 SourceMeter at a frequency of 15 Hz. The uncertainty is calculated as the standard deviation of the measurements when the helicon is not running. The uncertainty ranges from ± 0.5 to 2.3 mN with an average value of ± 1.9 mN. A water-cooled copper shroud surrounds the thrust stand components to maintain thermal equilibrium.

The thrust stand chiller is first run at 17°C overnight to bring the system to thermal equilibrium. VTF-1 is pumped down to a base pressure of 1.5×10^{-5} torr. The thrust stand is turned on and given 1 h to settle at a zero point and then calibrated. After calibration, the cold gas thrust is measured. The RF system is then set at 300 W to create the plasma. The two solenoids are then powered to provide the set magnetic field. The matching network is tuned to match to the plasma, and the RF power is set. The thrust stand is given 2 min to settle, and then the RF is turned off, with another 2 min of settling time. The difference in the thrust stand response between the plasma on and plasma off is the helicon plasma thrust contribution. The total thrust is the combination of the cold gas thrust and the helicon plasma thrust. The solenoids are then shut off, and the plasma is restarted, repeating the process for each power level (eight total) for a given frequency and mass flow rate. The procedure is then repeated for the next set of operating conditions. Thus, calibration occurs for every eight data points, or once every 80 min.

2. *Retarding Potential Analyzer*

The ion energy distribution of the thruster plume is measured with an RPA [32–34]. The RPA consists of four grids and a collector coaxially aligned within and isolated from a stainless steel cylinder. In order from aperture toward the collector, they are the floating, electron repulsion, ion repulsion, and electron suppression grids. The floating grid has no active potential applied and becomes charged to the floating potential. This serves to reduce perturbations in the plasma caused by the presence of the other biased grids. The electron repulsion grid is negatively biased with respect to chamber ground to repel plasma electrons and prevents them from reaching the collector and reducing the effective collection current. The ion repulsion grid is positively biased with respect to chamber ground to retard ions and controls what ion energies are capable of reaching the collector. The electron suppression grid has a negative potential relative to ground to repel secondary electrons emitted due to ion collisions with the collector. Because the ion repulsion grid controls the ion current collection, the probe acts as a high-pass filter, allowing only ions with energies higher than the ion repulsion grid potential to pass through to the collector. By sweeping the potential of ion repulsion grid V_{IRG}, a plot of collected ion current I_c as a function of the applied potential can be created. The negative derivative of the I–V characteristic is proportional to the ion energy distribution.

The RPA is mounted 45 cm downstream of the exit plane of the discharge chamber along the centerline of the device. At this distance, the RPA is removed far enough downstream to avoid disturbing the plasma yet is close enough to maintain a sufficient signal-to-noise ratio. The helicon is turned on using the preceding procedure and set to a given power, frequency, and magnetic field. The electron suppression and repulsion grids are biased 50 V below chamber ground. The ion repulsion grid bias is swept through a range of 0–100 V in 0.5 V increments six times using a Keithley 2410 SourceMeter with an accuracy of 0.12% [35]. The current collected by the probe is measured with a Keithley 6485 picoammeter, which has an accuracy of $\pm 0.1\%$ [36]. The six scans are then averaged to generate an overall I–V trace. A locally weighted scatter plot smoothing algorithm is used to smooth the data. Smoothing the data creates additional uncertainty, which is estimated as the standard deviation between the raw average and the smoothed line. The added uncertainty ranged from 1 to 7%, depending on how rough the raw average line is. It should be noted that thrust and ion energy profiles were not measured simultaneously but at different times at the same operating conditions.

III. Experimental Results

Figure 5 shows the thrust contour of the device as a function of power and magnetic field at three different mass flow rates at 11.9 MHz. At 150 G and mass flow rates 3.0 and 4.5 mg/s for RF powers greater than 675 and 590 W, respectively, the plasma did not have a stable match and could not be maintained long enough to measure thrust. Figure 6 shows the thrust at 13.56 MHz and 1.5 mg/s. Thrust appears to be sensitive to three parameters: RF power, magnetic field, and mass flow rate. Because of the relatively large values of the uncertainty in the measurements, it is difficult to make any comparison of the relative impact of each parameter, but power seems to have the largest effect on thrust. Any change in thrust due to a change in frequency cannot be determined with the given data.

There are two other performance parameters of interest for any thruster: thrust efficiency η_t and specific impulse I_{sp} of the device. The thrust efficiency of the thruster is defined as

$$\eta_t = \frac{T^2}{2\dot{m}P_{\mathrm{in}}} \tag{2}$$

where t is the thrust, $\dot{m}$ is the mass flow rate, and P_{in} is the total input power. The total input power consists of the RF power propagated through the antenna, the RF power loss in the transmission line, and the power used to run the solenoids. The latter two are dependent on the specific experimental setup used, and so for the sake of comparison with other work only the transmitted RF power is used in Eq. (2). As a reminder, the transmitted RF power is determined by measuring forward power at the amplifier and correcting for power losses in the cable up to the antenna. For this calculation, the matching network is assumed to be lossless.

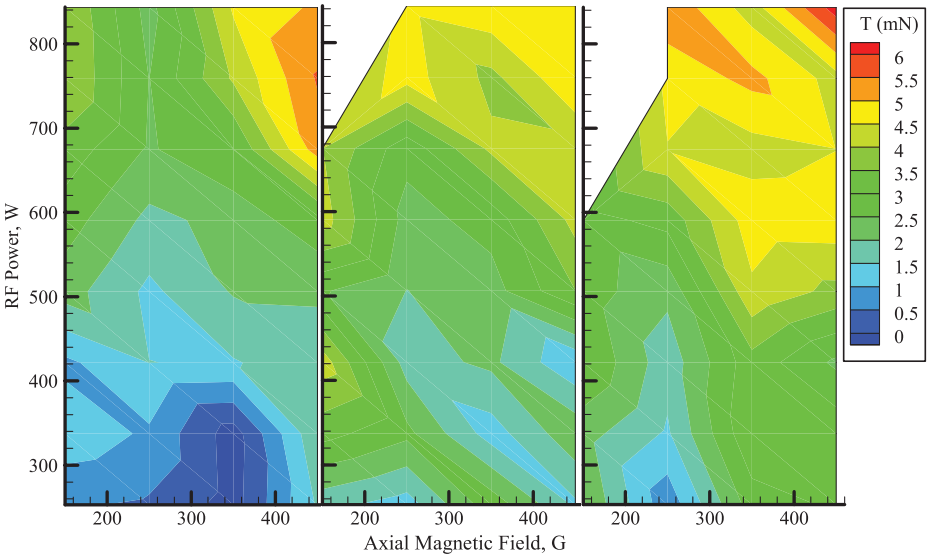

Fig. 5 Helicon thrust contour as a function of power and magnetic field for 11.9 MHz Ar, 1.5 mg/s (left), 3.0 mg/s (center), and 4.5 mg/s (right). Average uncertainty is ±1.9 mN.

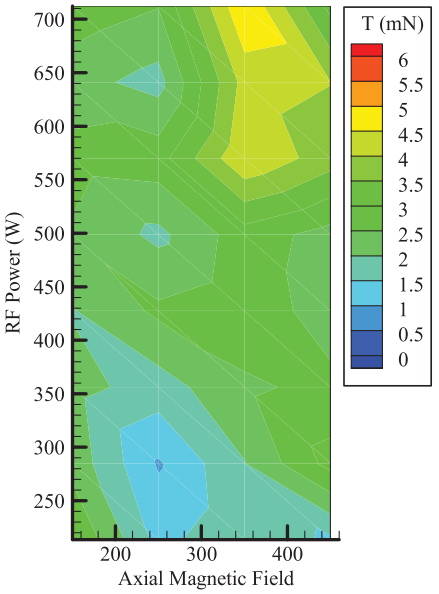

Fig. 6 Helicon thrust contour as a function of power and magnetic field for 13.56 MHz Ar, 1.5 mg/s. Average uncertainty is ±1.9 mN.

Figures 7 and 8 show the thrust efficiency of the device at different mass flow rates, powers, and magnetic fields. Thrust efficiency is very low, with a weak dependency on RF power. Uncertainty in the thrust efficiency is dominated by the uncertainty in the thrust measurements and is on average ±180% of the value.

The other performance parameter of interest is the specific impulse, defined as

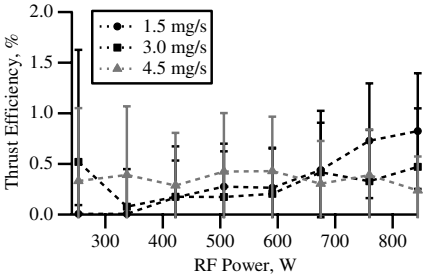

Fig. 8 Thrust efficiency as a function of power and mass flow for 350 G Ar, 11.9 MHz, 2.0–2.6 × 10^{-5} torr.

$$I_{sp} = \frac{T}{\dot{m}g} \tag{3}$$

where g is the acceleration due to gravity. The specific impulse of the device is shown in Figs. 9 and 10. Again, the large uncertainty prevents making many definitive statements beyond a weak correlation between the specific impulse and power. Figure 10 does show that at high power the specific impulse increases with decreased mass flow rate.

The resulting ion energy distribution from the RPA is shown in Fig. 11, with each distribution normalized by the maximum current collected by the RPA. The distributions show two primary peaks: the lower of the two corresponds to the plasma potential, and the higher-energy peak corresponds to the ion beam potential [17,22,24,25]. The difference in potential between these two peaks is the beam voltage. The magnetic field strength has a particularly strong effect on the plasma potential, the beam voltage, and the relative prevalence of the two energy populations. At 150 G, the plasma potential ranges between 20 and 25 V, the beam voltage is mostly between 35 and

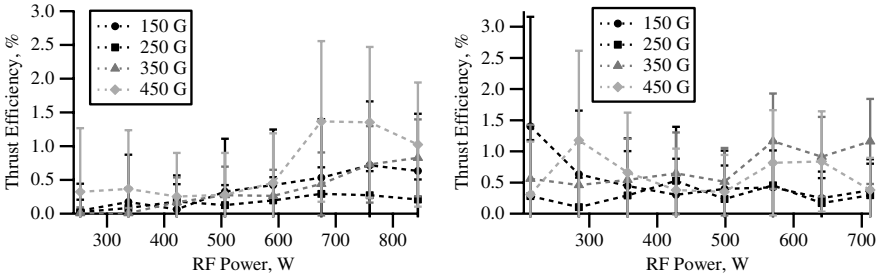

Fig. 7 Thrust efficiency as a function of power and magnetic field for 1.5 mg/s Ar, 2.0 × 10^{-5} torr, 11.9 MHz (left) and 13.56 MHz (right).

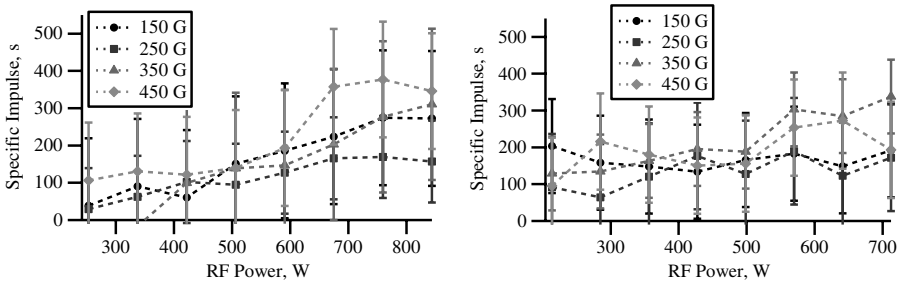

Fig. 9 Specific impulse as a function of power and magnetic field for 1.5 mg/s Ar, 2.0×10^{-5} torr, 11.9 MHz (left) and 13.56 MHz (right).

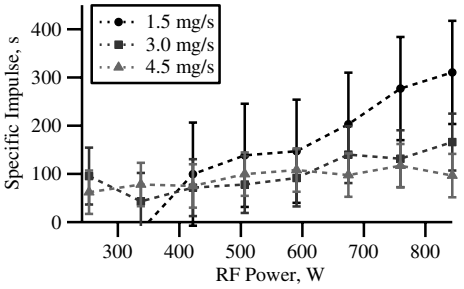

Fig. 10 Specific impulse as a function of power and mass flow rate for 350 G; 11.9 MHz; 2.0, 2.3, and 2.6×10^{-5} torr for 1.5, 3.0, and 4.5 mg/s flow rates, respectively.

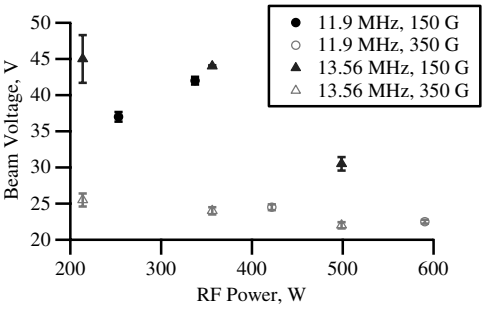

Fig. 12 Beam voltage as a function of frequency, power, and magnetic field 45 cm downstream of the exit plane on the centerline for 1.5 mg/s Ar, 2.0×10^{-5} torr.

45 V, and the beam population is relatively low. At 350 G, the plasma potential increases to 30–40 V, the beam voltage drops to around 25 V, and the beam population is equal to or greater than the low-energy population. Another observation is that at 150 G increasing RF power increases the size of the beam population, whereas at 350 G increasing RF power decreases the beam population. The beam voltages and their corresponding uncertainties are plotted in Fig. 12.

The plasma potentials and beam voltages observed in the 350 G case are similar to what is found in the literature. Previous plasma potentials ranged from about 30 V measured by Charles et al. [16] to about 50 V measured by Takahashi et al. [24] and Ling et al. [22], whereas the beam voltages were between 15 V with Pottinger et al. [25] and 30 V with Takahashi et al. [24]. It is worth noting that whereas these similarities exist for the 350 G case they do not hold for the 150 G case; furthermore, all four of the previous studies were conducted with magnetic field strengths in the range of 138–200 G. As has already been observed, the magnetic field has a strong impact on the behavior of the plasma potential and beam voltage; however, the data only match what is found previously at a higher magnetic field strength. This suggests that the relationship between ion energy and magnetic field strength is also dependent on other parameters.

Because the preceding studies were conducted using different devices at different operating conditions, it is beneficial to examine any other commonalities that may exist. One common parameter between those studies that differs with the one presented here is the vacuum vessel used. Takahashi et al. [24] and Ling et al. [22] performed their studies in a 1-m-diam by 1.4-m-long chamber with

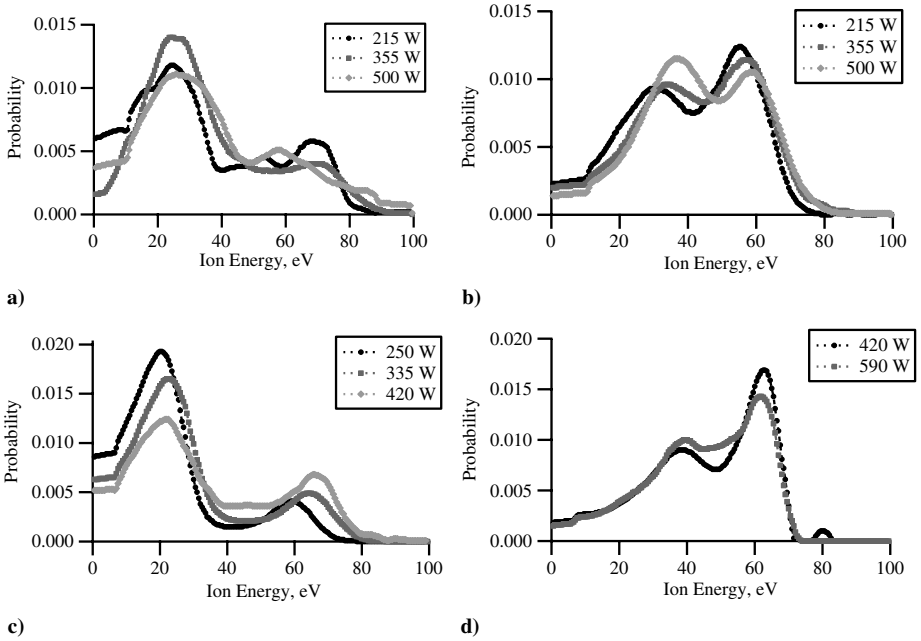

Fig. 11 Ion energy distributions 45 cm downstream of the exit plane for 1.5 mg/s Ar, 2.0×10^{-5} torr: a) 150 G, 13.56 MHz; b) 350 G, 13.56 MHz; c) 150 G, 11.9 MHz; and d) 350 G, 11.9 MHz.

operating pressures of 0.6 and 0.3 mtorr, respectively; Pottinger et al. [25] tested in a similarly sized 1.2-m-diam by 1.2-m-long chamber at an operating pressure of 0.5 mtorr; Charles et al. [16] used a 0.3-m-diam by 0.3-m-long expansion chamber at the end of the helicon at a pressure of 7×10^{-5} torr. In comparison, this study was performed in a 4-m-diam by 7-m-long chamber at an operating pressure of 2×10^{-5} torr. The combination of a lower operating pressure and a larger separation between the helicon and the grounded chamber wall means the downstream plume behavior is closer to that of in-space conditions by reducing charge exchange collisions with neutrals and plume interaction with the chamber wall.

The second distinction between previous studies and this work is the difference in propellant flow rates. Charles et al. [16] and Pottinger et al. [25] used about 4 sccm of xenon and 16 sccm of krypton, respectively, whereas Takahashi et al. [24] and Ling et al. [22] used about 20 sccm and 8 sccm of argon, respectively. For comparison, this work used a flow rate of 50 sccm during RPA measurements. However, Ling et al. and Charles et al. [16] used discharge chambers of nearly identical dimensions as the one used in this study, whereas Pottinger et al. [25] and Takahashi et al. [24] used discharge chambers with diameters of 8 and 6.4 cm, respectively. By particle conservation and assuming isothermal expansion, the pressure should scale as

$$p \sim \frac{Q}{d^2}\sqrt{m} \tag{4}$$

where Q is the propellant volumetric flow rate, d is the diameter of the discharge chamber, and m is the mass of the propellant atom. Using Eq. (4) and the operating conditions of the various experiments, the relative pressures inside the discharge chamber fit into two groups: the first is composed of the works of Pottinger et al. [25], Takahashi et al. [24], and this study; the other is composed of work done by Charles et al. [16] and Ling et al. [22]. One of the conditions for the formation of the double layer is a pressure less than about 1 mtorr [18,37], which would imply a distinction between the results of the two groups. However, because there is no clear distinction in the behavior of the ion energy distribution and operating conditions, it is likely that other parameters beyond discharge pressure have a pronounced effect on the double layer formation. Because there are such wide disparities in the different operating conditions of all the studies, definitive conclusions cannot yet be made.

IV. Discussion

Fine comparisons of the parametric effects of the operating conditions are difficult to make due to the large uncertainty in the data. The thrust measurement uncertainty is on average about ±90%, and the efficiency and the specific impulse have similarly large uncertainties because they are values derived from thrust measurements. The large uncertainty in the thrust measurements is due to the sensitivity of the thrust stand to vibrations. The load spring used in the thrust stand is one variable to control vibrations, with a looser spring to reduce vibrations. However, for heavier loads a stiffer load spring is needed to restrict thrust stand deflection, which increases sensitivity to vibrations. Generally, this is mitigated by the fact that a heavier thruster produces higher thrust. In this case, the helicon source has a mass of about 35 kg, which is comparable to a Hall effect thruster but with a much lower thrust. As a comparison, a T-140 Hall thruster has 200 mN of thrust and an uncertainty of ±2.3 mN, which is only 1.1% of the measured value [31]; the helicon has a thrust of 5 mN and an uncertainty of ±1.9 mN, which is 38% of the measured value. The uncertainty can be reduced by decreasing the mass of the helicon, the primary contributors of which are the solenoids. However, reducing the number of turns in the magnets would decrease the range of field strengths available for operation. An additional source of uncertainty in the efficiency calculations that is unknown is the amount of RF power that is coupled to the solenoid mounts. It is possible that some of the power capacitively couples to the cylindrical tube that the wire is wrapped around, which can then capacitively couple to the thrust stand, which is grounded.

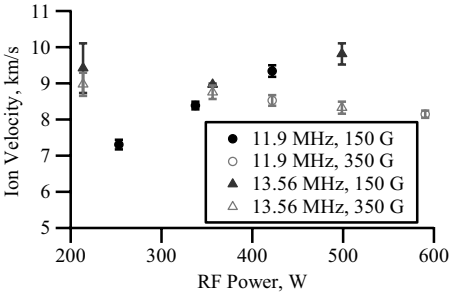

Fig. 13 Average ion exit velocity as a function of power, frequency, and magnetic field for 1.5 mg/s Ar, 2.0×10^{-5} torr.

Although a finer parametric study cannot be performed, a closer examination of the magnetic field effects is worthwhile. Despite the magnetic field having a pronounced effect on the beam voltage, is does not have a similarly noticeable effect on thrust. There are two values that are of interest for propulsion application: the average ion exit velocity and the ion beam current. Instead of using a singular ion exit velocity based on the beam voltage, an average ion exit velocity can be calculated from the ion energy distribution. For this, it is assumed that the low-energy population corresponds to ions at the plasma potential and higher-energy ion population is due to acceleration [17]. Therefore, the center of the first peak corresponds to the plasma potential, and only ions past that energy are accelerated. From the data in Fig. 11, the average ion exit velocity can be calculated using the equation

$$\bar{v}_i = \frac{\sum_{j=k+1}^{100} x_j (2e(V_j - V_p)/m_i)^{1/2}}{\sum_{j=k+1}^{100} x_i} \{k | V_k = V_p\} \tag{5}$$

where x_j is the probability at each voltage, V_j is the voltage of the jth term of the series, and V_p is the plasma potential. Figure 13 shows the calculated average ion exit velocity. At 150 G, this average velocity increases with power, whereas at 350 G velocity decreases with power. This follows from the observation noted earlier that at 150 G increasing power increases the high-energy ion population, whereas at 350 G increasing power decreases the high-energy ion population. Furthermore, for the 13.56 MHz case the average velocity for 350 G is lower than at 150 G, and the same is true for the 11.9 MHz case where overlapping data are available.

Because there are no azimuthal measurements of the downstream current density, a value of the total beam current is not available. Instead, the maximum centerline current collected by the RPA is used as a representative measure of the centerline beam current. Because the RPA collects ions from both populations, the current is weighted by the fraction of ions that exceed the plasma potential as shown in Eq. (6):

$$I_{c,w} = I_{c,\max} \sum x_j \{j | V_j > V_p\} \tag{6}$$

This weighted centerline ion current, $I_{c,w}$, is plotted in Fig. 14 at each operating condition. At 150 G, the current collected is about half that

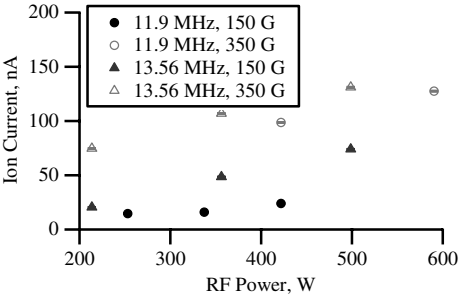

Fig. 14 Weighted centerline ion current as a function of power, frequency, and magnetic field for 1.5 mg/s Ar, 2.0×10^{-5} torr, 45 cm downstream of exit plane.

of the 350 G case, although in both cases ion current increases with RF power.

There are two observable effects as the magnetic field is decreased: an increase in beam voltage and a decrease in centerline ion current. Two possible reasons for a decrease in centerline ion current are a decrease in ion generation and an increase in beam divergence. Even if the cause cannot be definitively known from the data available, both result in decreased thrust, whereas an increase in beam voltage generally results in higher average ion velocity and higher thrust. The competing effects of changing the magnetic field explain why the impact of magnetic field on thrust is small compared with its effect on beam voltage or centerline ion current.

From the data collected, the primary impediment to the use of a helicon source as a thruster is the very low thrust efficiency. Although an exact breakdown of the loss sources is not available, a problem that can be identified is the low beam voltage. Previous studies measured beam voltages ranging from 15 to 30 V, whereas here the beam voltage was found between 25 and 45 V. The electrical efficiency of a thruster is the ratio of the beam power to the sum of the beam power and power spent creating the ions. Assuming that the total cost per ion is some x factor multiplied by the ionization cost of the propellant, ε^+, then the electrical efficiency is

$$\eta_e = \frac{I_b V_b}{I_b V_b + I_b x \varepsilon^+} \tag{7}$$

FAs an example, in an idealized dc thruster discharge the energy cost per ion is 7.5 times the ionization energy of the atom [38]. Assuming this ideal discharge at the maximum beam voltage measured, the maximum possible efficiency would be around 28%. Therefore, even if a helicon plasma source has high ionization efficiency, the electrical efficiency, and thus thrust efficiency, is limited by the amount of energy spent in ion acceleration relative to ion creation. Because of the low beam voltages measured, a helicon plasma source in its current form at these operating conditions is unsuitable as a thruster. Unless an operating condition can be found that greatly increases the beam voltage, development of a thruster that includes a helicon source will require the addition of an acceleration stage that can independently increase the beam voltage.

V. Conclusions

The thrust of a helicon plasma source is measured across a range of mass flow rates, magnetic field strengths, RF powers, and RF frequencies. This is the first study to be done at near-space conditions below 3×10^{-5} torr, in a chamber an order of magnitude larger than the device, on an inverted pendulum thrust stand. Maximum thrust is found to be 6.3 mN at a specific impulse of 140 s and a maximum specific impulse of 380 s at 5.6 mN. Thrust efficiency is found to be low, never exceeding 1.4%. Thrust and thrust efficiency are primarily limited by low ion beam current and low beam voltage, which ranged between 20 and 45 V. The low beam voltage demonstrates that the most likely method for increasing the thrust and thrust efficiency of a helicon plasma source used in a propulsive application is an added acceleration stage.

Acknowledgments

The authors would like to thank American Pacific in Space Propulsion for their support, the Georgia Institute of Technology Aerospace Engineering Machine Shop for fabrication and hardware support, as well as the students of the Georgia Institute of Technology High-Power Electric Propulsion Laboratory for additional assistance.

References

[1] Chen, F. F., "Plasma Ionization by Helicon Waves," *Plasma Physics and Controlled Fusion*, Vol. 33, No. 4, 1991, pp. 339–364. doi:10.1088/0741-3335/33/4/006

[2] Boswell, R. W., "Very Efficient Plasma Generation by Whistler Waves near the Lower Hybrid Frequency," *Plasma Physics and Controlled Fusion*, Vol. 26, No. 10, 1984, pp. 1147–1162. doi:10.1088/0741-3335/26/10/001

[3] Chen, F. F., and Boswell, R. W., "Helicons: the Past Decade," *IEEE Transactions on Plasma Science*, Vol. 25, No. 6, 1997, pp. 1245–1257. doi:10.1109/27.650899

[4] Chen, F. F., "Experiments on Helicon Plasma Sources," *Journal of Vacuum Science and Technology*, Vol. 10, No. 4, 1992, pp. 1389–1401.

[5] Borg, G. G., and Boswell, R. W., "Power Coupling to Helicon and Trivelpiece–Gould Modes in Helicon Sources," *Physics of Plasmas*, Vol. 5, No. 3, 1998, pp. 564–571. doi:10.1063/1.872748

[6] Shamrai, K. P., and Taranov, V. B., "Volume and Surface RF Power Absorption in a Helicon Plasma Source," *Plasma Sources Science and Technology*, Vol. 5, No. 3, 1996, pp. 474–491. doi:10.1088/0963-0252/5/3/015

[7] Kimura, S., and Ikoma, H., "Fowler–Nordheim Current Injection and Write/Erase Characteristics of Metal-Oxide–Nitride-Oxide–Si Structure Grown with Helicon-Wave Excited Plasma Processing," *Journal of Applied Physics*, Vol. 85, No. 1, 1999, pp. 551–557. doi:10.1063/1.369488

[8] Winglee, R., Ziemba, T., Giersch, L., Prager, J., Carscadden, J., and Robertson, B. R., "Simulation and Laboratory Validation of Magnetic Nozzle Effects for the High Power Helicon Thruster," *Physics of Plasmas*, Vol. 14, No. 6, 2007, pp. 063501-1–063501-14. doi:10.1063/1.2734184

[9] Hwang, Y. S., Hong, I. S., and Eom, G. S., "Conceptual Design of a Helicon Ion Source for High-Current DC Accelerators," *Review of Scientific Instruments*, Vol. 69, No. 3, 1998, pp. 1344–1348.

[10] Hong, I. S., Hwang, Y. S., Lee, G. H., Kim, D. Y., Won, H. Y., Eom, G. S., and Choe, W., "Ion-Beam Characteristics of Novel Helicon Ion Sources for Different Plasma Parameters," *Review of Scientific Instruments*, Vol. 71, No. 3, 2000, pp. 1385–1388. doi:10.1063/1.1150467

[11] Mordyk, S., Miroshnichenko, V., Shulha, D., and Storizhko, V., "Investigation of Helicon Ion Source Extraction Systems," *Review of Scientific Instruments*, Vol. 79, No. 2, 200802B707-1–02B707-4.

[12] Gilland, J., "Application of a Helicon Discharge to Electric Propulsion," AIAA Paper 1998-3934, 1998.

[13] Gilland, J., "The Potential for Compact Helicon Wave Sources for Electric Propulsion," *27th International Electric Propulsion Conference*, Pasadena, CA, IEPC Paper 2001-210, 15–19 October, 2001.

[14] Ziemba, T., Carscadden, J., Slough, J., Prager, J., and Winglee, R., "High Power Helicon Thruster," AIAA Paper 2005-4119, 2005.

[15] Charles, C., Alexander, P., Costa, C., Sutherland, O., Boswell, R. W., Pfitzner, L., Franzen, R., Kingwell, J., Parfitt, A., Frigot, P. E., Gonzalez del Amo, J., Gengembre, E., and Saccoccia, E., "Helicon Double Layer Thrusters," *International Electric Propulsion Conference*, IEPC Paper 2005-290, 2005.

[16] Charles, C., Boswell, R. W., and Lieberman, M. A., "Xenon Ion Beam Characterization in a Helicon Double Layer Thruster," *Applied Physics Letters*, Vol. 89, No. 26, 2006, pp. 261503-1–261503-3. doi:10.1063/1.2426881

[17] West, M. D., Charles, C., and Boswell, R. W., "Testing a Helicon Double Layer Thruster Immersed in a Space-Simulation Chamber," *Journal of Propulsion and Power*, Vol. 24, No. 1, 2008, pp. 134–141. doi:10.2514/1.31414

[18] Charles, C., "A Review of Recent Laboratory Double Layer Experiments," *Plasma Sources Science and Technology*, Vol. 16, No. 4, 2007, pp. R1–R25. doi:10.1088/0963-0252/16/4/R01

[19] Charles, C., and Boswell, R. W., "Current-Free Double-Layer Formation in a High-Density Helicon Discharge," *Applied Physics Letters*, Vol. 82, No. 9, 2003, pp. 1356–1358. doi:10.1063/1.1557319

[20] Longmier, B. W., Bering, E. A. III., Carter, M. D., Cassady, L. D., Chang-Díaz, F. R., Glover, T. W., Hershkowitz, N., Ilin, A. V., McCaskill, G. E., Olsen, C. S., and Squire, J. P., "Ambipolar Ion Acceleration in an Expanding Magnetic Nozzle," *Plasma Sources Science and Technology*, Vol. 20, No. 1, 2011, p. 015007. doi:10.1088/0963-0252/20/1/015007

[21] Cox, W., Charles, C., Boswell, R. W., and Hawkins, R., "Spatial Retarding Field Energy Analyzer Measurements Downstream of a Helicon Double Layer Plasma," *Applied Physics Letters*, Vol. 93, No. 7, 2008, pp. 071505-1–071505-3. doi:10.1063/1.2965866

[22] Ling, J., West, M. D., Lafleur, T., Charles, C., and Boswell, R. W., "Thruster Measurements in a Low-Magnetic Field High-Density Mode in the Helicon Double Layer Thruster," *Journal of Physics D: Applied*

Physics, Vol. 43, No. 30, 2010, pp. 325203-1–325203-9. doi:10.1088/0022-3727/43/30/305203

[23] Longmier, B., Cassady, L. D., Ballenger, M. G., Chang-Díaz, F. R., Glover, T. W., Ilin, A. V., McCaskill, G. E., Olsen, C. S., Squire, J. P., and Bering, E. A. III., "VX-200 Magnetoplasma Thruster Performance Results Exceeding Fifty-Percent Thruster Efficiency," *Journal of Propulsion and Power*, Vol. 27, No. 4, 2011, pp. 915–920.

[24] Takahashi, K., Lafleur, T., Charles, C., Alexander, P., Boswell, R. W., Perren, M., Laine, R., Pottinger, S., Lappas, V., Harle, T., and Lamprou, D., "Direct Thrust Measurement of a Permanent Magnet Helicon Double Layer Thruster," *Applied Physics Letters*, Vol. 98, No. 14, 2011, pp. 141503-1–141503-3. doi:10.1063/1.3577608

[25] Pottinger, S., Lappas, V., Charles, C., and Boswell, R. W., "Performance Characterization of a Helicon Double Layer Thruster Using Direct Thrust Measurements," *Journal of Applied Physics D*, Vol. 44, No. 23, 2011, pp. 235201-1–235201-5.

[26] Chi, K., Sheridan, T. E., and Boswell, R. W., "Resonant Cavity Modes of a Bounded Helicon Discharge," *Plasma Sources Science and Technology*, Vol. 8, No. 3, 1999, pp. 421–431. doi:10.1088/0963-0252/8/3/312

[27] *Vacuum Measurement*, Varian, Inc., 2005, http://www.varianinc.com/cgibin/nav?products/vacuum/measure/index&cid=IPMHIKJQFO [accessed 2009].

[28] MKS Product Specifications, *MKS 1179A Instruction Manual*, MKS Instruments, 2000, p. 57.

[29] Keickhafer, A. W., and Walker, M. L. R., "RF Power System for Thrust Measurements of a Helicon Plasma Source," *Review of Scientific Instruments*, Vol. 81, No. 7, 2010, pp. 075106-1–075106-8.

[30] Cheetham, A. D., and Rayner, J. P., "Characterization and Modeling of a Helicon Plasma Source," *Journal of Vacuum Science and Technology A*, Vol. 16, No. 5, 1998, pp. 2777–2784. doi:10.1116/1.581421

[31] Xu, K. G., and Walker, M. L. R., "High-Power, Null-Type, Inverted Pendulum Thrust Stand," *Review of Scientific Instruments*, Vol. 80, No. 5, 2009, pp. 055103-1–055103-6. doi:10.1063/1.3125626

[32] Hofer, R. R., "Development and Characterization of High-Efficiency, High Specific Impulse Xenon Hall Thrusters," Ph.D. Dissertation, Dept. of Aerospace Engineering, Univ. of Michigan, Ann Arbor, MI, 2004.

[33] King, L. B., "Transport-Property and Mass Spectral Measurements in the Plasma Exhaust Plume of a Hall-Effect Space Propulsion System," Ph.D. Dissertation, Dept. of Aerospace Engineering, Univ. of Michigan, Ann Arbor, MI, 1998.

[34] Hutchinson, I. H., *Principles of Plasma Diagnostics*, Cambridge Univ. Press, Cambridge, 1987.

[35] Keithley Product Specifications, Keithley 2400 Series Sourcemeter Instruction Manual, Keithley Instruments, 1998, p. 508.

[36] Keithley Product Specifications, *Keithley 6485 Picoammeter Instruction Manual*, Keithley Instruments, 2001, p. 220.

[37] Charles, C., and Boswell, R. W., "Laboratory Evidence of a Supersonic Ion Beam Generated by a Current-Free 'Helicon' Double-Layer," *Physics of Plasmas*, Vol. 11, No. 4, 2004, pp. 1706–1714. doi:10.1063/1.1652058

[38] Goebel, D. M., and Katz, I., *Fundamentals of Electric Propulsion: Ion and Hall Thrusters*, edited by Yuen, J. H., Space Science and Technology Series, Jet Propulsion Lab., Pasadena, CA, p. 98.

A. Gallimore
Associate Editor